

Article

Facile Fabrication of Porous MoSe₂/Carbon Microspheres via the Aerosol Process as Anode Materials in Potassium-Ion Batteries

Du Yeol Jo ¹ and Seung-Keun Park ^{1,2,3,*} ¹ Department of Advanced Materials Engineering, Chung-Ang University, 4726, Seodong-daero, Daedeok-myeon, Anseong 17546, Republic of Korea² Department of Intelligent Energy and Industry, Chung-Ang University, 84 Heukseok-ro, Dongjak-gu, Seoul 06974, Republic of Korea³ Western Seoul Center, Korea Basic Science Institute, 150 Bugahyeon-ro, Seodaemun-gu, Seoul 03759, Republic of Korea

* Correspondence: skpark09@cau.ac.kr

Abstract: Recently, potassium-ion batteries (KIBs) have attracted significant interest due to a number of factors, including the growing demand for energy and limited lithium resources. However, their practical use is hampered by poor cycling stability due to the large size of K⁺. Therefore, it is critical to develop a structural design that effectively suppresses large volume changes. This study presents a simple method of using a salt template to fabricate porous microspheres (p-MoSe₂@C MS) of MoSe₂ and a carbon matrix as anode materials in KIBs. These microspheres have a distinct porous design, with uniformly distributed MoSe₂ nanocrystals embedded in the carbon matrix to prevent MoSe₂ overgrowth due to material diffusion during heat treatment. The manufacturing process combined one-step spray drying with recyclable NaCl as a hard template. Through a two-step thermal process under an inert atmosphere, the initial dextrin, NaCl, and Mo salt microspheres were converted into a p-MoSe₂@N MS composite. The carbon structure derived from the dextrin maintained the shape of the microspheres when NaCl was removed, ensuring no overgrowth of MoSe₂. This well-designed porous structure improves the interaction with the electrolyte, facilitating the transport of ions and electrons and reducing the K⁺ diffusion distances. In addition, the porous carbon structure accommodates large volume changes during cycling and maintains its structural strength. As a result, p-MoSe₂@C MS composite exhibits superior electrochemical properties, with remarkable capacity, long-term cycling stability (193 mA h g⁻¹ after 500 cycles at 2.0 A g⁻¹), and rate capability.



Citation: Jo, D.Y.; Park, S.-K. Facile Fabrication of Porous MoSe₂/Carbon Microspheres via the Aerosol Process as Anode Materials in Potassium-Ion Batteries. *Batteries* **2024**, *10*, 25. <https://doi.org/10.3390/batteries10010025>

Academic Editor: Torsten Brezesinski

Received: 1 December 2023

Revised: 3 January 2024

Accepted: 6 January 2024

Published: 9 January 2024



Copyright: © 2024 by the authors. Licensee MDPI, Basel, Switzerland. This article is an open access article distributed under the terms and conditions of the Creative Commons Attribution (CC BY) license (<https://creativecommons.org/licenses/by/4.0/>).

1. Introduction

Over the past decade, the increasing demand for sustainable and highly efficient energy storage has stimulated advances in Li-ion batteries (LIBs) [1,2]. However, the limited supply and uneven distribution of lithium, which make it expensive, pose significant challenges for scaling LIB adoption [3,4], thus increasing the urgency of developing affordable and efficient alternative energy storage solutions. Potassium-ion batteries (KIBs) and sodium-ion batteries (SIBs), which function similarly to LIBs, are recognized as excellent substitutes for LIBs due to the abundant resources of potassium and sodium [5,6]. Among them, KIBs have distinct advantages over SIBs. The significantly lower Lewis acidity of K⁺ compared to Li⁺ and Na⁺ in KIBs allows a higher dissolution of K⁺ [7]. In addition, the reduced dissolution energy of K⁺ allows faster ion diffusion at the electrolyte–electrode interface [8]. Even though KIBs operate via a mechanism similar to that of LIBs, they have faster ion movement in an electrolyte owing to a low K/K⁺ redox potential (−2.92 V), resulting in a higher energy density [9]. However, large K⁺ ions, nearly twice the size of lithium ions,

impart greater stress on the electrode material, resulting in slower diffusion during charge and discharge cycles [10].

Layered transition-metal dichalcogenides, known for their narrow-bandgap semiconducting capabilities, large interlayer spacing, and two-dimensional (2D) lamellar formations, are becoming increasingly popular as effective anodes for energy-storage applications [11]. In particular, MoSe₂, with its unique sandwich-like configuration consisting of a Mo-Se monolayer bound by strong in-plane covalent bonds and layered by weak van der Waals forces [12,13], is prominent for its ability to store Na⁺ and K⁺. Despite its advantages, MoSe₂ faces challenges such as structural degradation owing to substantial volume fluctuations during ion insertion/extraction and limited electrical conductivity, resulting in poor cycle life and rate capability [14,15]. Therefore, implementing a simple approach that counteracts electrode damage due to stress and creates a cushioning space to manage volume changes and improve electrochemical kinetics is crucial.

Integrating carbon-based materials such as amorphous carbon, graphene, and carbon nanotubes (CNTs) with layered transition-metal dichalcogenides, has proven to be an effective solution for overcoming these obstacles [16–18]. These carbon compounds enhance electrical conductivity and structural integrity while offering numerous other benefits [19]. In particular, amorphous carbon, rich in defects, can accommodate large amounts of K⁺ ions, while its inherent structural elasticity helps compensate for volume shifts. Consequently, applying amorphous carbon coatings to MoSe₂ crystals improved both the capacity and cycling stability of KIBs.

In addition to the integration of carbon-based materials, the architectural design of MoSe₂ also plays a critical role in improving the rate performance and cycle life of KIBs [20]. Current research efforts are driving the development of spherical porous MoSe₂ structures [21,22]. These novel designs have the dual advantage of reducing the mechanical stress due to volume changes and maximizing the surface area, resulting in better electrolyte penetration and superior ion diffusion rates [23].

However, several previous studies required an additional step in their methods, involving the synthesis of solid templates, such as SiO₂ or latex beads, to aid in the development of porous MoSe₂ [24]. This additional step complicates and lengthens the fabrication process, rendering the fabrication of porous structures complex and time-consuming, thus highlighting an urgent need to refine and simplify this process.

In this study, we present an innovative technique that uses a spray-drying process to produce a unique porous microsphere (MS), p-MoSe₂@C MS, composed of MoSe₂ and an amorphous carbon matrix. These materials were specifically designed as anode materials for advanced KIBs. We fabricated this unique structure using readily available and inexpensive NaCl salt. The primary microspheres were formed by spray drying a water-based solution containing dextrin, NaCl, and molybdenum salts, followed by carbonization in an inert environment. The amorphous carbon matrix derived from dextrin was instrumental in maintaining the structural integrity of the particles during NaCl extraction, effectively circumventing common overgrowth problems associated with MoSe₂. The porous carbon matrix also counteracted the significant volume changes that MoSe₂ underwent during cycling, thereby strengthening its structure. These composites exhibited impressive properties, such as high specific capacity, long-term cycling stability, and exceptional rate performance, when tested as anodes in KIBs.

2. Experimental Procedures

A water-based solution containing 0.014 M ammonium molybdate ((NH₄)₆Mo₇O₂₄, SAMCHUN, Seoul, Republic of Korea), 30 g L⁻¹ dextrin ((C₆H₁₀O₅)_n, SAMCHUN, Republic of Korea), and 50 g L⁻¹ sodium chloride (NaCl, JUNSEI) was used for spray drying. During spray drying, the fluid nozzle pressure was maintained at 2.0 bar, with an outlet temperature of 100 °C. The resulting precursor powder was subjected to heat treatment for 3 h after reaching 650 °C at a temperature rise rate of 5 °C min⁻¹ in an Ar atmosphere. The carbonized powder was then stirred in water for 1 h to dissolve the NaCl and then dried

at room temperature. Subsequent selenization was then performed at 450 °C for 6 h with the same temperature rise rate in an argon environment to produce p-MoSe₂@C MS complexes. For comparison, an aqueous solution without NaCl was prepared from the same colloidal solution. The MoSe₂@C MS was then produced by spray drying, carbonization, and selenization under the same conditions except for the washing step.

3. Results and Discussion

Scheme 1 provides a detailed outline of the process used to create novel porous microspheres. This fabrication technique requires the precise control of several critical steps. First, in the spray-drying phase (Scheme 1-1), a water-based solution containing specific proportions of Mo salt, dextrin, and NaCl template was rapidly dried. The subsequent carbonization stage (Scheme 1-2), performed in an inert environment, converts dextrin into a carbon matrix and the Mo salt into molybdenum oxide. Next, the NaCl was washed with deionized water (Scheme 1-3), resulting in porous microspheres reinforced by the carbon matrix. This NaCl extraction process is easy to implement and allows NaCl recycling by drying the extracted solution. The final step, selenization (Scheme 1-4), completed the synthesis of the unique p-MoSe₂@C MS composite.



Scheme 1. Schematic illustration of p-MoSe₂@C MS preparation.

Scanning electron microscopy (SEM) was used to investigate the unique contributions of NaCl to the spray solution by focusing on the morphological features of the microspheres (Figures 1 and 2). The microspheres with added NaCl exhibited perfectly spherical shapes with smooth surfaces (Figure 1a,b); this structure remained intact after carbonization (Figure 1c,d). After simple water-based NaCl removal, the internal NaCl crystals were completely eliminated, creating porous voids inside the particles (Figure 1e,f). These pores remained intact even after selenization, demonstrating the effectiveness of this simple method in maintaining the porous structure (Figure 1g,h). The high surface area of the particles allowed for a uniform distribution of MoSe₂ crystals, and the use of an NaCl template in the spray-drying process successfully prevented the excessive growth of MoSe₂ during selenization. In contrast, microspheres prepared without NaCl exhibited highly wrinkled surfaces (Figure 2a,b). This structure persisted after carbonization (Figure 2c,d), with the excessive growth of MoSe₂ evident on the surfaces of these particles after selenization (Figure 2e,f). These morphological observations indicate that the NaCl template helps create a porous structure and effectively disperses the Mo salt throughout the process. In addition, the X-ray diffraction (XRD) patterns (Figure S1) of the p-MoSe₂@C MS composite were consistent with the crystalline phase of MoSe₂, as indicated by PDF#01-072-1420 and 01-077-1715.

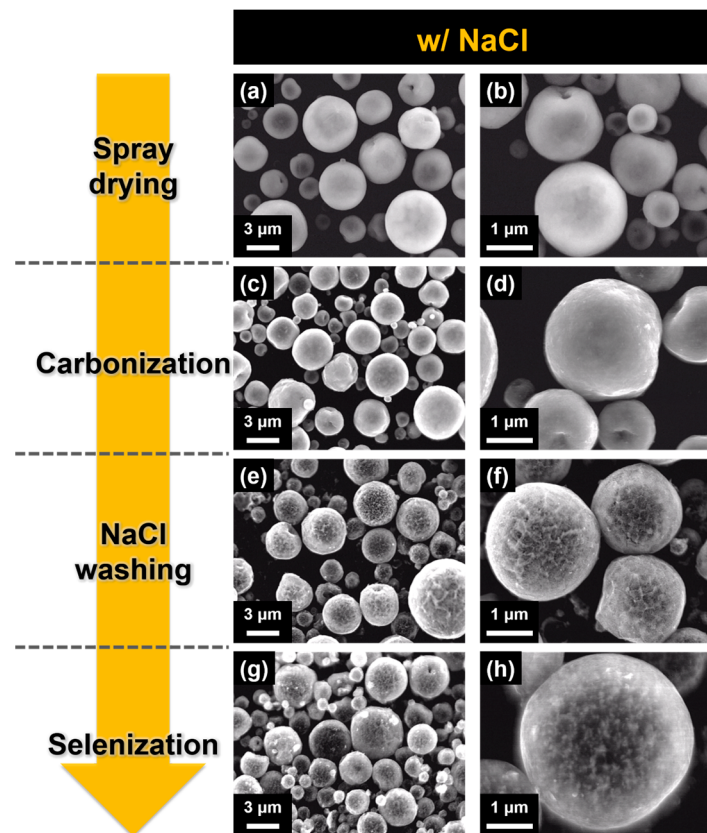


Figure 1. SEM images of samples prepared by using different preparation methods: (a,b) after spray drying, (c,d) after carbonization, (e,f) after NaCl washing, and (g,h) after selenization.

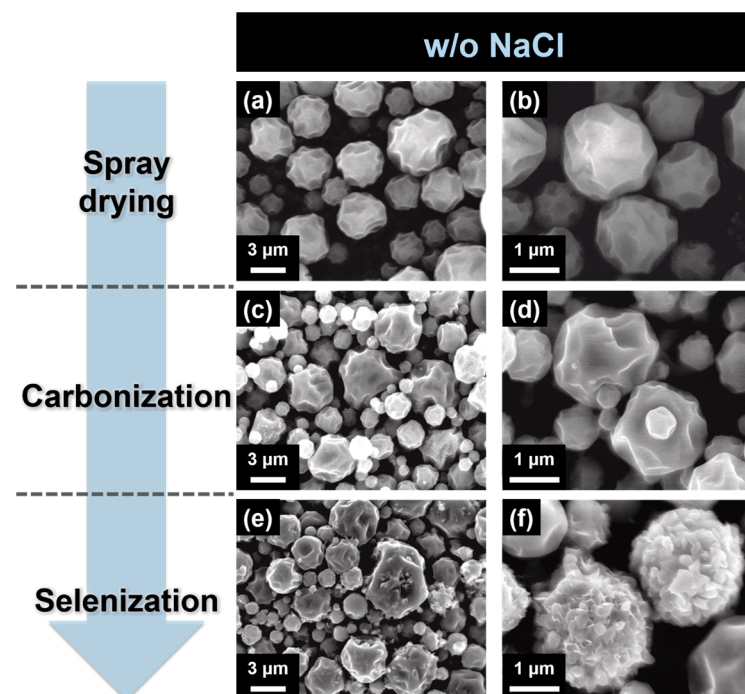


Figure 2. SEM images of samples prepared by using different preparation methods: (a,b) after spray drying, (c,d) after carbonization, and (e,f) after selenization.

The transmission electron microscopy (TEM, supported by the Korea Basic Science Institute Daegu Center) images in Figure 3 provide detailed insights into the morphology

and crystalline structure of the p-MoSe₂@C MS composite. Each microsphere clearly shows a spherical shape (Figure 3a), with the porous nature highlighted by the different contrasts in the images (Figure 3b). The high-resolution (HR) TEM image (Figure 3c) reveals a lattice gap of 0.24 nm, typical of the (103) plane of MoSe₂. In addition, the selected-area electron diffraction (SAED) pattern (Figure 3d) was consistent with the XRD pattern in Figure S1, confirming the crystalline facets of MoSe₂. The energy distribution X-ray (EDX) image (Figure 3e) shows a uniform distribution of Mo, Se, and C elements within the microspheres, indicating a homogeneous composition of MoSe₂ and carbon. In addition, the SEM (Figure 1g,h) and TEM (Figure 3a,b) images show that these microspheres have a carbon-based matrix. In light of these results, it is believed that the MoSe₂ nanosheets are well integrated with the porous carbon matrix in the p-MoSe₂@C MS composite. The results of thermogravimetric (TG) analysis, which aimed to measure the carbon quotient of the p-MoSe₂@C MS composites, are shown in Figure S2. The initial weight increase was associated with oxidation, resulting in the formation of MoO₃ and SeO₂. Based on the conclusion that the residue after the analysis was pure MoO₃, the final carbon content was determined to be 16.9 wt.%.

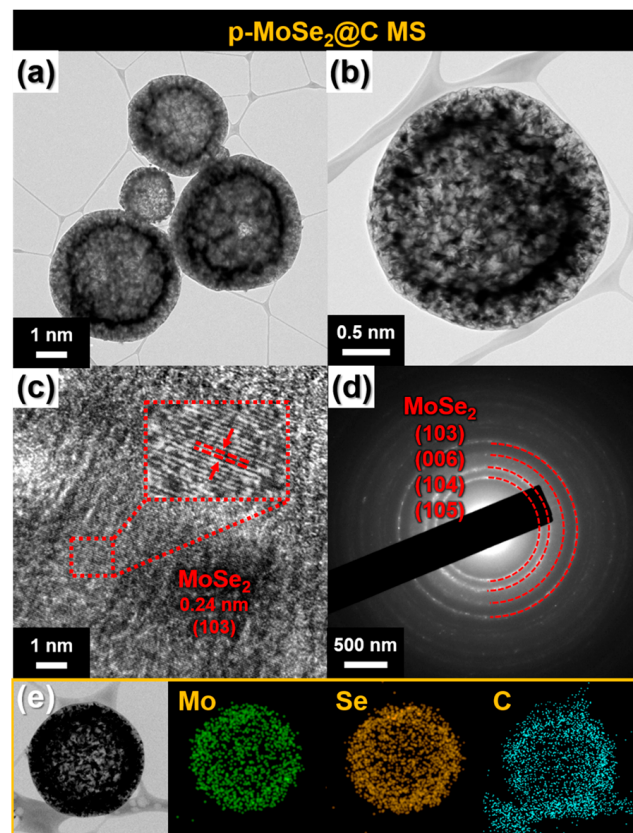


Figure 3. (a,b) TEM images, (c) HR-TEM image, (d) SAED pattern, and (e) EDX mapping images of p-MoSe₂@C MS.

Figure 4 provides a detailed analysis of the chemical composition and oxidation states of the p-MoSe₂@C MS composite as revealed by X-ray photoelectron spectroscopy (XPS). The overall survey spectrum (Figure 4a) meticulously detailed the elemental constituents, indicating the presence of C, Mo, and Se within the composite. The HR Mo 3d spectrum (Figure 4b) shows prominent peaks at 232.18 eV and 229.18 eV, associated with the Mo 3d_{3/2} and Mo 3d_{5/2} states, respectively [25]. Similarly, the HR Se 3d spectrum (Figure 4c) shows peaks for Se 3d_{5/2} (55.58 eV) and Se 3d_{3/2} (54.68 eV), highlighting the established MoSe₂ phase [26]. The HR C 1s spectrum (Figure 4b) shows peaks at 286.08 eV and 284.68 eV, representing the C–O–C and C–C bond structures, respectively.

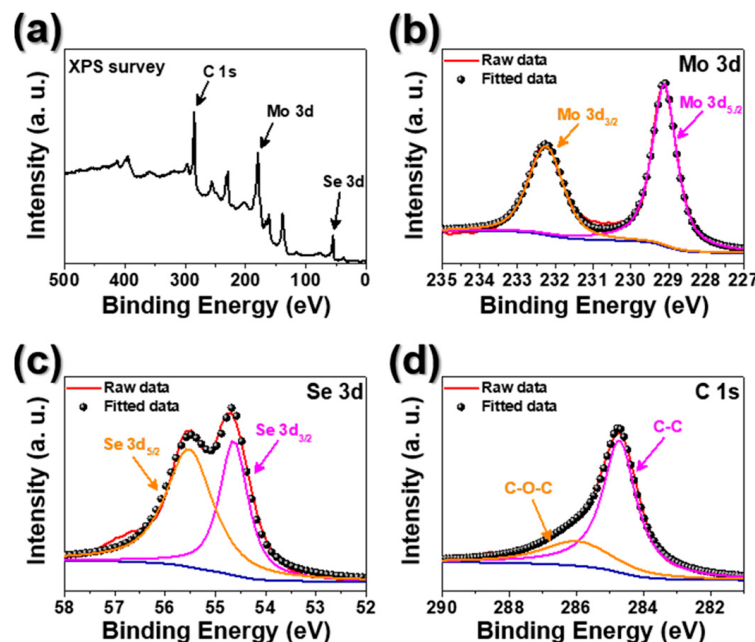


Figure 4. XPS result of p-MoSe₂@C MS: (a) survey spectra, (b) Mo 3d, (c) Se 3d, and (d) C 1s spectrum.

Figure S3 presents the Raman spectra of the p-MoSe₂@C MS composite, showing two significant peaks at 244 cm^{-1} and 303 cm^{-1} associated with the A_{1g} and E_{2g}^1 modes (Figure S3a), thus confirming the presence of MoSe₂ [27]. In addition, the carbon component in the composite is indicated by the D and G bands at 1324 cm^{-1} and 1590 cm^{-1} . Notably, as seen in Figure S3b, the intensity ratio (I_D/I_G) of these bands was greater than 1.0, suggesting that the conversion of dextrin into an amorphous carbon matrix, which is influenced by the low carbonization temperature, results in numerous defects. These defects in the amorphous carbon structure provide more active sites than those in graphitic structures, which are important for managing repeated volume changes [28].

Analysis of the N₂ adsorption/desorption isotherms, shown in Figure 5, provides important information about the surface areas of the p-MoSe₂@C MS and MoSe₂@C MS composites. As seen in Figure 5a, the surface areas of these composites were found to be $62.7\text{ m}^2\text{ g}^{-1}$ and $1.8\text{ m}^2\text{ g}^{-1}$, respectively, suggesting that the larger surface area of the p-MoSe₂@C MS composite is mainly attributed to the pores formed during the NaCl templating process. The MoSe₂@C MS composite has a much smaller surface area than its p-MoSe₂@C MS counterpart. In addition, analysis of the pore size distribution, as shown in Figure 5b, indicated that the p-MoSe₂@C MS composite contained pores ranging from 20 to 100 nm. This distribution is consistent with the size of the NaCl template, confirming that these pores developed in the spaces left by the removed NaCl.

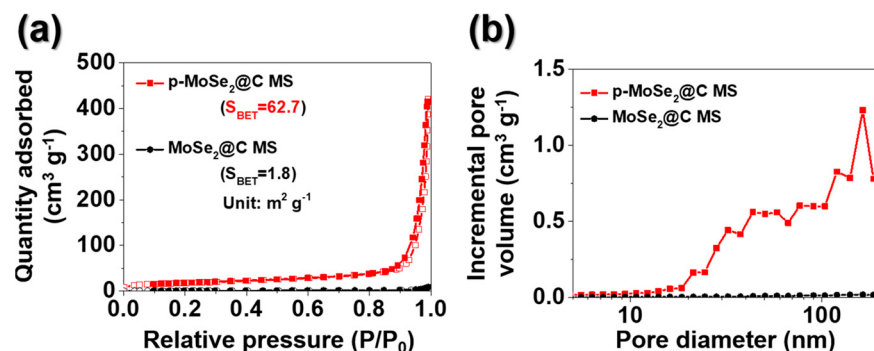


Figure 5. (a) N₂ adsorption and desorption isotherm curves and (b) BJH pore-size distribution graphs of p-MoSe₂@C MS and MoSe₂@C MS.

Figure 6 shows the results of the K^+ storage mechanism in the p-MoSe₂@C MS electrode. The cyclic voltammetry (CV) data shown in Figure 6a, performed at a scan rate of 0.01 mV s^{-1} , reveal the impressive structural integrity of the electrode, as evidenced by the consistent trajectory of the curves beyond the first cycle. The first cathodic sweep shows a pronounced peak from about 0.2 to 1.0 V, representing the successive processes of K^+ intercalation, conversion, and alloying reactions that culminate in the formation of Mo and K₂Se [29]. In addition, a peak at 0.01 V is observed, indicating the encapsulation of K^+ within the amorphous carbon matrix [30]. In particular, the peak of the first CV curve decreases in subsequent cycles, a change attributed to the initial capacity loss resulting from the formation of an irreversible SEI layer [29]. Conversely, the CV curves for the second and fifth cycles maintain consistent widths, indicating that capacity is highly reversible during subsequent cycles. On the anodic side, the peak at 1.7 V signals reversion to the original MoSe₂ structure. However, the MoSe₂@C MS electrode, as shown in Figure S4, showed overlapping and less distinct peaks, suggesting difficulties in K^+ storage owing to the overgrowth of MoSe₂.

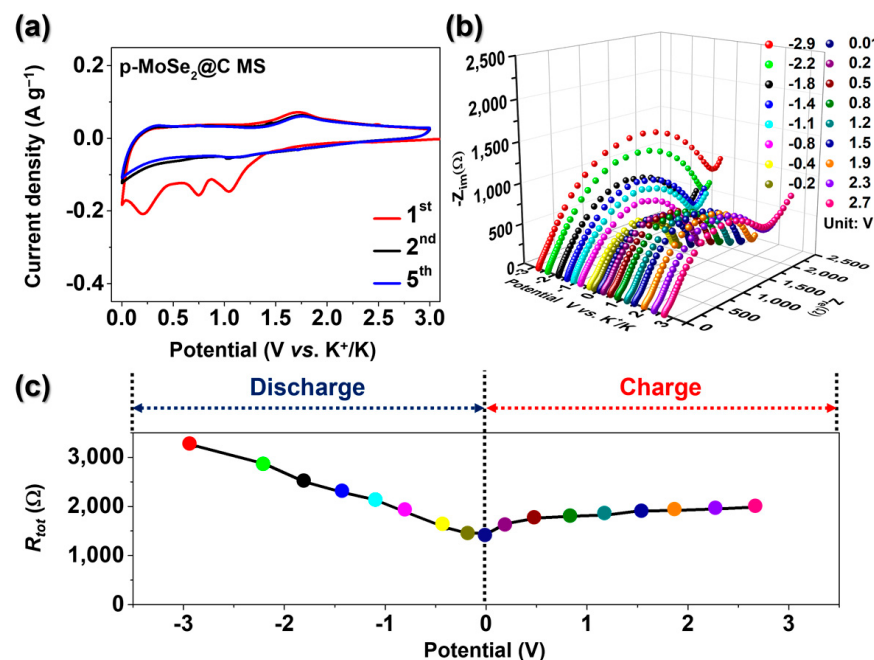


Figure 6. Charge/discharge mechanism at KIBs of p-MoSe₂@C MS: (a) CV curves and (b) the Nyquist plots at preselected potential levels, and (c) the calculated EIS results.

In situ electrochemical impedance spectroscopy (EIS) was used to meticulously examine the variations in the total resistance during the initial cycle of the p-MoSe₂@C MS electrode, as shown in Figure 6b,c. Nyquist plots were methodically obtained at specific potential stages (Figure 6b) and analyzed using a Randle-type circuit model (Figure S5). During the first discharge phase, the total resistance (R_{tot}) consistently decreased, suggesting the formation of a SEI layer (Figure 6c). In contrast, during the subsequent charging phase, the charge-transfer resistance (R_{ct}) increased progressively, attributed to the conversion of metal nanoparticles into their respective metal selenides, characterized by relatively low electrical conductivities [31].

In the initial charge–discharge analysis shown in Figure S6, the p-MoSe₂@C MS electrode exhibited an initial discharge capacity of $639.2 \text{ mA h g}^{-1}$ and an initial coulombic efficiency (CE) of 73%, with this initial CE largely influenced by the irreversible formation of the SEI layer [32]. The porous nature of the p-MoSe₂@C MS electrode, which contributes to its lower initial CE, provides extensive contact with the electrolyte and numerous active sites. Despite this, the p-MoSe₂@C MS electrode consistently achieved a high CE exceeding 90% in subsequent cycles, highlighting its remarkable reversibility over multiple charge–

discharge cycles. Furthermore, the p-MoSe₂@C MS electrode shows that both the plateau and CV peaks (Figure 6a) in the initial charge–discharge reaction curve occur in the same voltage range. This suggests a sequence of conversion reactions. In contrast, the MoSe₂@C MS electrode shows no CV peaks in the voltage range indicative of a conversion reaction (Figure S4). This absence of peaks is due to the excessive overgrowth of MoSe₂ particles in the MoSe₂@C MS electrode, which limits their reactivity with K⁺. These results confirm the good agreement between the initial charge–discharge curve and the CV curve.

Figure 7 shows the K⁺ storage performance of each electrode. The cycling stability was tested at a steady current density of 0.5 A g⁻¹ after an initial stabilization period at a lower density of 0.1 A g⁻¹ for five cycles, as shown in Figure 7a. Both the p-MoSe₂@C MS and MoSe₂@C MS electrodes show an increase in capacity over 50 cycles, a phenomenon associated with polymer gel network formation and electrode activation [33]. The slower diffusion of the larger potassium ions into the electrode is a major factor in the gradual capacity increase over extended cycles [34]. Notably, the p-MoSe₂@C MS electrode maintained a high stable discharge capacity of 300.3 mA h g⁻¹ after 300 cycles, in contrast to the significant capacity degradation observed in the MoSe₂@NC electrode. In addition, the long-term performance of the p-MoSe₂@C MS electrode was evaluated at a higher current density of 2.0 A g⁻¹, as shown in Figure 7b. This electrode showed consistent cycling capability, maintaining a high discharge capacity of 192.7 mA h g⁻¹ even after 500 cycles. The well-designed porous structure of the p-MoSe₂@C MS electrode effectively prevented the excessive growth of MoSe₂ particles, allowing the volume expansion of the particles to be uniformly distributed within the carbon matrix. Conversely, the MoSe₂@C MS electrode experienced short circuits when the current density was rapidly increased from 0.1 to 2.0 A g⁻¹, as shown in Figure 7c. These results emphasize the inferior K⁺ storage capability of the MoSe₂@C MS electrode, mainly attributed to the overgrowth of MoSe₂ particles.

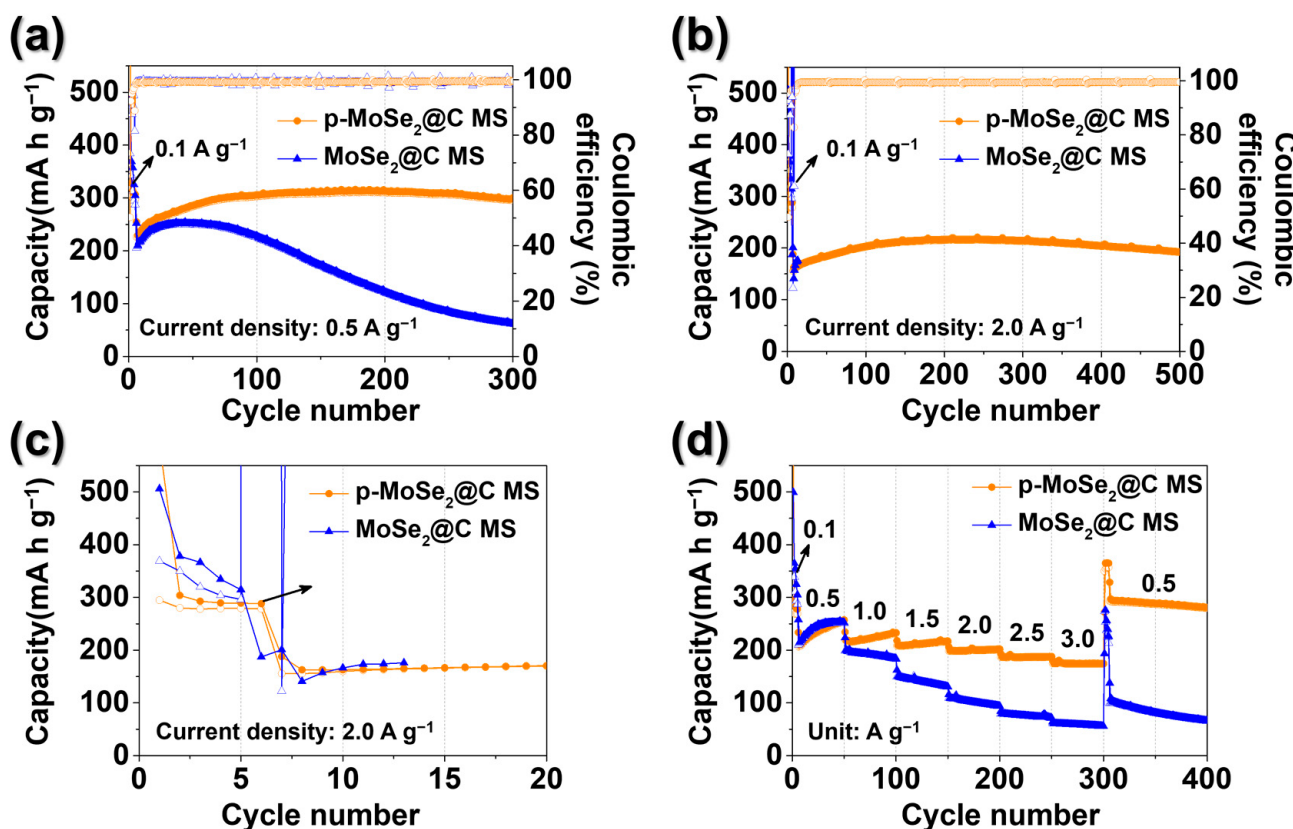


Figure 7. K⁺ storage performance of p-MoSe₂@C MS and MoSe₂@C MS electrodes: cycling stability at current density of (a) 0.5 A g⁻¹ and (b), (c) 2.0 A g⁻¹, and (d) rate capability.

As shown in Figure S7, post-cycle scanning electron microscopy (SEM) analysis was performed after 200 cycles to examine the structural conditions of each electrode. The SEM images of the p-MoSe₂@C MS electrode, especially Figure S7a,b, clearly show that the particles retained their spherical shape even after extensive cycling. In addition, the surface of particles after cycling is thicker than the original particles (Figure 1g,h), and the unique porous structure has disappeared, which can be ascribed to the formation of a SEI layer. In contrast, the MoSe₂@NC electrode exhibited significant structural degradation because of its intrinsic instability, as shown in Figure S7c,d. The morphological changes observed in each electrode after 200 cycles are strongly consistent with the respective cycling performance data, as shown in Figure 7a. In particular, the unique porous structure of the p-MoSe₂@C MS electrode played a critical role in accommodating repeated volume fluctuations, thereby ensuring its ability to maintain stable performance and structural integrity over extended cycling periods. In Table S1, the electrochemical performance of the p-MoSe₂@C MS electrode is compared with other Mo-based anodes previously reported for KIBs, highlighting its outstanding performance.

Figure 7d shows the results of the rate capability evaluation results for each electrode at different current densities. In these evaluations, the p-MoSe₂@C MS electrode consistently showed a higher capacity at all current densities tested. Notably, the MoSe₂@C MS electrode did not regain its original capacity after the current density was reset to its initial value. In contrast, the p-MoSe₂@C MS electrode excelled at high current densities and reliably recovered its capacity, thus highlighting the robust structural stability of the porous designs. Moreover, the MoSe₂@C MS electrode consistently exhibited the lowest capacity over the entire current density range, mainly attributed to the reduced electrochemical activity of the overgrown MoSe₂ particles.

CV analysis was performed over scan rates of 0.1–2.0 mV s⁻¹ to investigate the electrochemical response dynamics of the electrodes, as shown in Figure 8. The slope (denoted as *b*) was determined using the mathematical relationship ($i = av^b$), which relates the current (*i*) to the scan rate (*v*) derived from the CV data [35]. A *b*-value of approximately 1.0 typically indicates that the electrochemical reaction is largely driven by a capacitive contribution process [36]. As shown in Figure 8c,d, the p-MoSe₂@C MS electrode consistently exhibited a *b*-value close to 1.0, particularly for the redox processes. Furthermore, at a scan rate of 2.0 mV s⁻¹, the capacitive contributions were 83% and 85% for the MoSe₂@C MS and p-MoSe₂@C MS electrodes, respectively, as highlighted in Figure 8e,f. Notably, the p-MoSe₂@C MS exhibited the highest capacitive contribution over all scan rates, as shown in Figure 8g,h, which is beneficial for the fast kinetics of K⁺ reactions, consistent with the results of the rate capability tests shown in Figure 7d. Interestingly, the magnitude of the capacitive contribution is closely related to the pore structure and crystal size of the active material [37]. Therefore, the p-MoSe₂@C MS electrode, characterized by its advanced pore structure and effective prevention of MoSe₂ particle overgrowth, exhibited more efficient K⁺ storage reaction kinetics.

Figure 9 presents a detailed analysis of the internal resistance of each electrode, both in the fresh state and after cycling. In the fresh state (Figure 9a), the charge-transfer resistance of the p-MoSe₂@C MS electrode was significantly lower than that of the MoSe₂@C MS electrode, indicating the superior interfacial kinetics of the p-MoSe₂@C MS electrode. After cycling, internal resistance decreased significantly, attributed to the formation of a SEI layer with high ionic conductivity on the surface of the electrode [38]. The Nyquist plots obtained after cycling consistently show a lower internal resistance for the p-MoSe₂@C MS sample (Figure 9b,c), indicating that the robustness of the electrode is maintained throughout the cycling process, consistent with the cycling performance data shown in Figure 7a. The unique porous structure of the electrode contributed to this result by enhancing structural integrity and improving electrolyte wettability, which, in turn, accelerated K⁺ movement. To further assess ion diffusion into the electrode, the slope was calculated based on the relationship between the phase angle and the real impedance component in the low-frequency region of the Nyquist plot (Figure 9d). The p-MoSe₂@C MS electrode showed

a lower slope, indicating more effective ion transfer to the electrode [39], reflecting the advantage of its well-developed porous structure in promoting efficient ion diffusion. In contrast, the overgrowth of MoSe₂ particles at the p-MoSe₂@C MS electrode hindered its electrochemical reaction with K⁺, resulting in suboptimal ion diffusion.

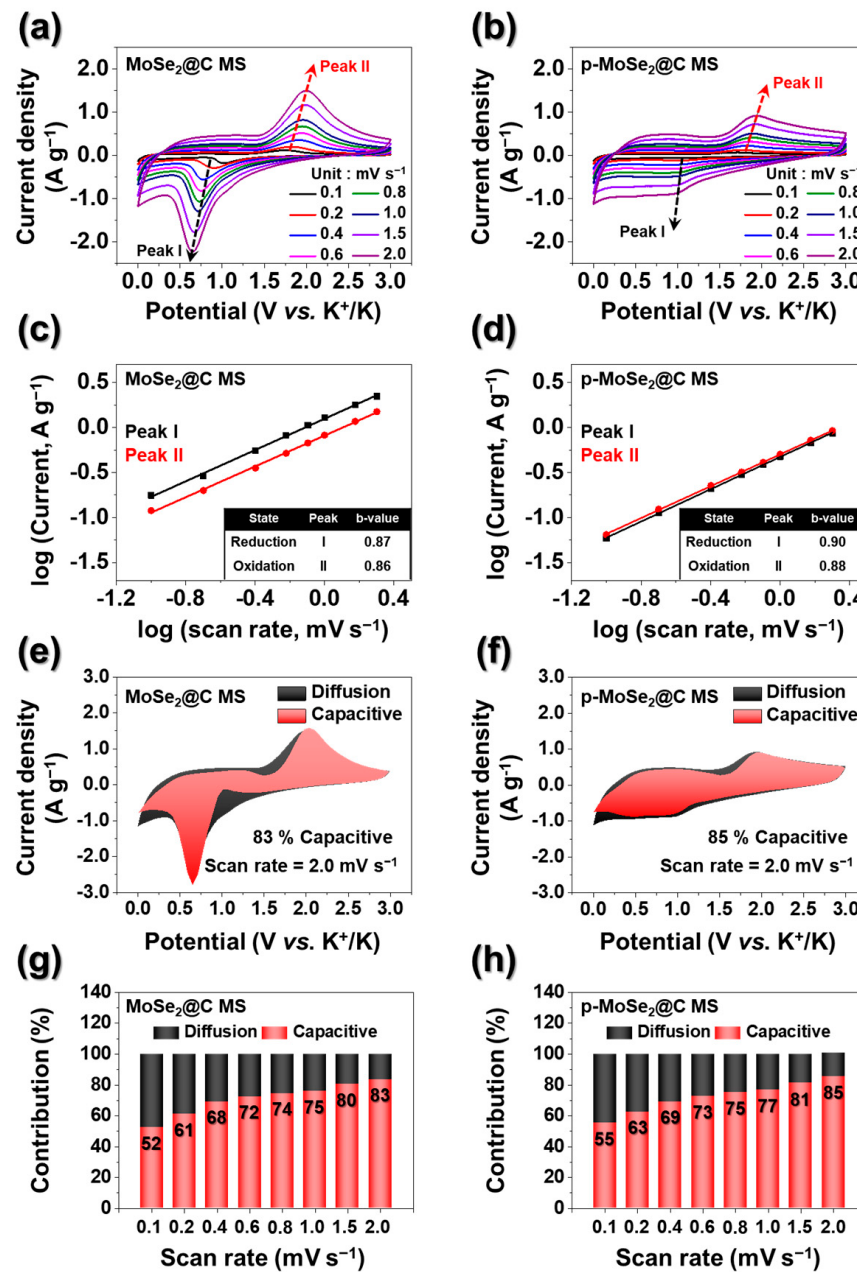


Figure 8. (a,b) CV curves at various scan rates, (c,d) *b*-value, (e,f) capacitive contributions at a scan rate of 2.0 mV s⁻¹, and (g,h) capacitive contribution at different scan rates of p-MoSe₂@C MS and MoSe₂@C MS electrodes.

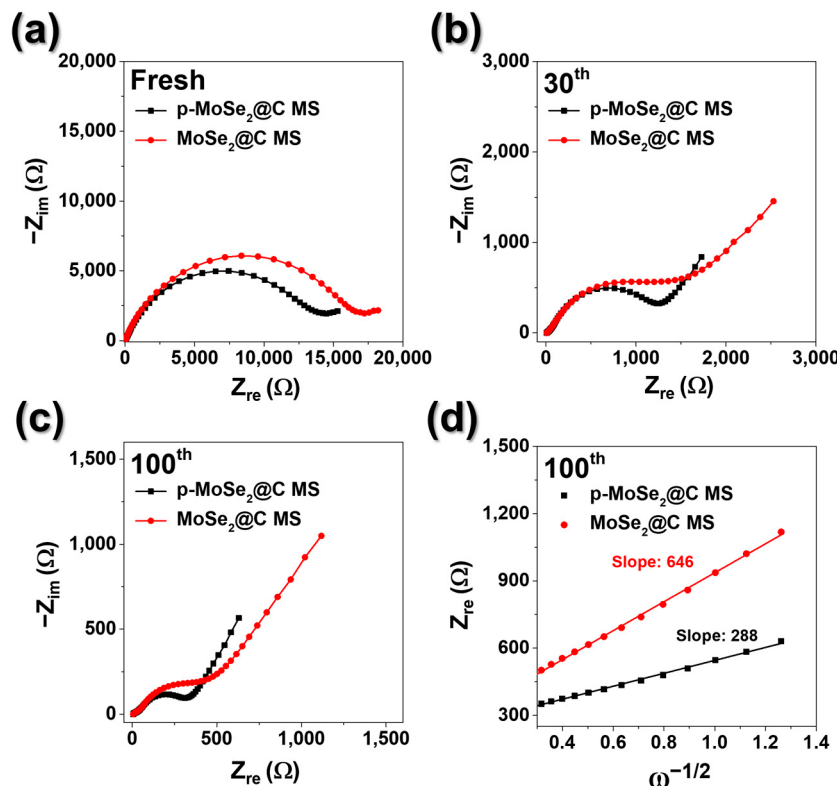


Figure 9. Nyquist plots of p-MoSe₂@C MS and MoSe₂@C electrodes: (a) at fresh cells, after (b) 30 and (c) 100 cycles, and (d) relationship between the Z_{re} and $\omega^{-1/2}$ after 100 cycles.

4. Conclusions

This paper presents an innovative salt-templating technique for preparing p-MoSe₂@C porous microspheres that show great potential as KIB anodes through an economical one-step spray-drying method using reusable NaCl templates. The prepared p-MoSe₂@C porous microspheres feature a unique design wherein uniform MoSe₂ nanocrystals are embedded within an amorphous carbon framework. This novel structure offers numerous advantages, including effective electrolyte penetration, minimized diffusion paths for potassium ions, and remarkable accommodation of volumetric changes during battery operation. Moreover, the p-MoSe₂@C microspheres exhibited promising electrochemical properties, highlighting their viability as a sustainable option for energy storage. This study highlights the importance of thoughtful design and synthesis techniques in developing advanced electrode materials, thereby contributing to the advancement of energy-storage systems.

Supplementary Materials: The following supporting information can be downloaded at: <https://www.mdpi.com/article/10.3390/batteries10010025/s1>; Figure S1: XRD patterns of p-MoSe₂@C MS and MoSe₂@C MS; Figure S2: TG curve of p-MoSe₂@C MS; Figure S3: Raman spectra of p-MoSe₂@C MS; Figure S4: CV curves of MoSe₂@C MS electrodes; Figure S5: Randle-type circuit model; Figure S6: The initial galvanostatic charge-discharge curves of p-MoSe₂@C MS and MoSe₂@C MS electrodes; Figure S7: SEM images after 200 cycles of p-MoSe₂@C MS and MoSe₂@C MS electrodes; Table S1: Electrochemical properties of various nanostructured Mo-based anode materials for potassium-ion batteries reported in the previous literatures.

Author Contributions: D.Y.J.: Conceptualization, Investigation, Data curation, Formal analysis, Writing—original draft. S.-K.P.: Supervision, Conceptualization, Funding acquisition, Writing—review & editing. All authors have read and agreed to the published version of the manuscript.

Funding: This research was supported by the Chung-Ang University Research Scholarship Grant in 2022 and National Research Foundation of Korea (NRF) grant funded by the Korean government (MSIT) (No. 2020R1C1C100337).

Data Availability Statement: Dataset available on request from the authors.

Conflicts of Interest: The authors declare that they have no known competing financial interests or personal relationships that could have appeared to influence the work reported in this paper.

References

- Xie, J.; Lu, Y.-C. A Retrospective on Lithium-Ion Batteries. *Nat. Commun.* **2020**, *11*, 2499. [[CrossRef](#)] [[PubMed](#)]
- Qiao, Y.; Deng, H.; He, P.; Zhou, H. A 500 Wh/kg Lithium-Metal Cell Based on Anionic Redox. *Joule* **2020**, *4*, 1445–1458. [[CrossRef](#)]
- Tarascon, J.-M. Is Lithium the New Gold? *Nat. Chem.* **2010**, *2*, 510. [[CrossRef](#)] [[PubMed](#)]
- Xu, H.; Yu, Y.; Wang, Z.; Shao, G. First Principle Material Genome Approach for All Solid-State Batteries. *Energy Environ. Mater.* **2019**, *2*, 234–250. [[CrossRef](#)]
- Ji, B.; Yao, W.; Zheng, Y.; Kidkhunthod, P.; Zhou, X.; Tunmee, S.; Sattayaporn, S.; Cheng, H.-M.; He, H.; Tang, Y. A Fluoroxalate Cathode Material for Potassium-Ion Batteries with Ultra-Long Cyclability. *Nat. Commun.* **2020**, *11*, 1225. [[CrossRef](#)] [[PubMed](#)]
- Zhu, Y.-H.; Zhang, Q.; Yang, X.; Zhao, E.-Y.; Sun, T.; Zhang, X.-B.; Wang, S.; Yu, X.-Q.; Yan, J.-M.; Jiang, Q. Reconstructed Orthorhombic V_2O_5 Polyhedra for Fast Ion Diffusion in K-Ion Batteries. *Chem.* **2019**, *5*, 168–179. [[CrossRef](#)]
- Zhang, Z.; Li, M.; Gao, Y.; Wei, Z.; Zhang, M.; Wang, C.; Zeng, Y.; Zou, B.; Chen, G.; Du, F. Fast Potassium Storage in Hierarchical $Ca_{0.5}Ti_2(PO_4)_3@C$ Microspheres Enabling High-Performance Potassium-Ion Capacitors. *Adv. Funct. Mater.* **2018**, *28*, 1802684. [[CrossRef](#)]
- Lei, K.; Li, F.; Mu, C.; Wang, J.; Zhao, Q.; Chen, C.; Chen, J. High K-Storage Performance Based on the Synergy of Dipotassium Terephthalate and Ether-Based Electrolytes. *Energy Environ. Sci.* **2017**, *10*, 552–557. [[CrossRef](#)]
- Kubota, K.; Dahbi, M.; Hosaka, T.; Kumakura, S.; Komaba, S. Towards K-Ion and Na-Ion Batteries as “Beyond Li-Ion”. *Chem. Rec.* **2018**, *18*, 459–479. [[CrossRef](#)]
- Deng, H.; Wang, L.; Li, S.; Zhang, M.; Wang, T.; Zhou, J.; Chen, M.; Chen, S.; Cao, J.; Zhang, Q.; et al. Radial Pores in Nitrogen/Oxygen Dual-Doped Carbon Nanospheres Anode Boost High-Power and Ultrastable Potassium-Ion Batteries. *Adv. Funct. Mater.* **2021**, *31*, 2107246. [[CrossRef](#)]
- Ge, J.; Fan, L.; Wang, J.; Zhang, Q.; Liu, Z.; Zhang, E.; Liu, Q.; Yu, X.; Lu, B. MoSe₂/N-Doped Carbon as Anodes for Potassium-Ion Batteries. *Adv. Energy Mater.* **2018**, *8*, 1801477. [[CrossRef](#)]
- Wu, Y.-C.; Liu, W.-R. Few-Layered MoSe₂ Ultrathin Nanosheets as Anode Materials for Lithium Ion Batteries. *J. Alloys Compd.* **2020**, *813*, 152074. [[CrossRef](#)]
- Zheng, C.; Wu, J.; Li, Y.; Liu, X.; Zeng, L.; Wei, M. High-Performance Lithium-Ion-Based Dual-Ion Batteries Enabled by Few-Layer MoSe₂/Nitrogen-Doped Carbon. *ACS Sustain. Chem. Eng.* **2020**, *8*, 5514–5523. [[CrossRef](#)]
- Ren, W.; Zhang, H.; Guan, C.; Cheng, C. Ultrathin MoS₂ Nanosheets@Metal Organic Framework-Derived N-Doped Carbon Nanowall Arrays as Sodium Ion Battery Anode with Superior Cycling Life and Rate Capability. *Adv. Funct. Mater.* **2017**, *27*, 1702116. [[CrossRef](#)]
- Morant-Giner, M.; Sanchis-Gual, R.; Romero, J.; Alberola, A.; García-Cruz, L.; Agouram, S.; Galbiati, M.; Padial, N.M.; Waerenborgh, J.C.; Martí-Gastaldo, C.; et al. Prussian Blue@MoS₂ Layer Composites as Highly Efficient Cathodes for Sodium- and Potassium-Ion Batteries. *Adv. Funct. Mater.* **2018**, *28*, 1706125. [[CrossRef](#)]
- Yi, Y.; Sun, Z.; Li, C.; Tian, Z.; Lu, C.; Shao, Y.; Li, J.; Sun, J.; Liu, Z. Designing 3D Biomorphic Nitrogen-Doped MoSe₂/Graphene Composites toward High-Performance Potassium-Ion Capacitors. *Adv. Funct. Mater.* **2020**, *30*, 1903878. [[CrossRef](#)]
- Tao, J.; Yan, Z.; Wang, D.; Zhong, W.; Yang, Y.; Li, J.; Lin, Y.; Huang, Z. Rational Designing of MoSe₂ Nanosheets in Carbon Framework for High-Performance Potassium-Ion Batteries. *Chem. Eng. J.* **2022**, *448*, 137658. [[CrossRef](#)]
- Su, C.; Ru, Q.; Gao, Y.; Shi, Z.; Zheng, M.; Chen, F.; Chi-Chung Ling, F.; Wei, L. Biowaste-Sustained MoSe₂ Composite as an Efficient Anode for Sodium/Potassium Storage Applications. *J. Alloys Compd.* **2021**, *850*, 156770. [[CrossRef](#)]
- Zhao, Z.; Hu, Z.; Liang, H.; Li, S.; Wang, H.; Gao, F.; Sang, X.; Li, H. Nanosized MoSe₂@Carbon Matrix: A Stable Host Material for the Highly Reversible Storage of Potassium and Aluminum Ions. *ACS Appl. Mater. Interfaces* **2019**, *11*, 44333–44341. [[CrossRef](#)]
- Zheng, J.; Wu, Y.; Sun, Y.; Rong, J.; Li, H.; Niu, L. Advanced Anode Materials of Potassium Ion Batteries: From Zero Dimension to Three Dimensions. *Nano-Micro Lett.* **2020**, *13*, 12. [[CrossRef](#)]
- Liu, Y.; Zhai, Y.; Wang, N.; Zhang, Y.; Lu, Z.; Xue, P.; Bai, L.; Guo, M.; Huang, D.; Bai, Z. Ultrathin MoSe₂ Nanosheets Confined in N-Doped Macroporous Carbon Frame for Enhanced Potassium Ion Storage. *ChemistrySelect* **2020**, *5*, 2412–2418. [[CrossRef](#)]
- Jiang, Q.; Wang, L.; Wang, Y.; Qin, M.; Wu, R.; Huang, Z.; Yang, H.-J.; Li, Y.; Zhou, T.; Hu, J. Rational Design of MoSe₂ Nanosheet-Coated MOF-Derived N-Doped Porous Carbon Polyhedron for Potassium Storage. *J. Colloid Interface Sci.* **2021**, *600*, 430–439. [[CrossRef](#)] [[PubMed](#)]
- Ruan, J.; Wu, X.; Wang, Y.; Zheng, S.; Sun, D.; Song, Y.; Chen, M. Nitrogen-Doped Hollow Carbon Nanospheres towards the Application of Potassium Ion Storage. *J. Mater. Chem. A* **2019**, *7*, 19305–19315. [[CrossRef](#)]
- Xia, G.; Wang, C.; Jiang, P.; Lu, J.; Diao, J.; Chen, Q. Nitrogen/Oxygen Co-Doped Mesoporous Carbon Octahedrons for High-Performance Potassium-Ion Batteries. *J. Mater. Chem. A* **2019**, *7*, 12317–12324. [[CrossRef](#)]
- Wang, F.; Li, Y.; Liang, X.; Liu, Y.; Chen, Q.; Chen, M. Inhibiting Structural Degeneration of MoSe₂ Anode with Dual-Layer Protection for Highly Robust Na-Ion Battery. *Mater. Chem. Phys.* **2022**, *278*, 125681. [[CrossRef](#)]

26. Truong, Q.D.; Kempaiah Devaraju, M.; Nakayasu, Y.; Tamura, N.; Sasaki, Y.; Tomai, T.; Honma, I. Exfoliated MoS₂ and MoSe₂ Nanosheets by a Supercritical Fluid Process for a Hybrid Mg–Li-Ion Battery. *ACS Omega* **2017**, *2*, 2360–2367. [CrossRef] [PubMed]
27. Mao, J.; Yu, Y.; Wang, L.; Zhang, X.; Wang, Y.; Shao, Z.; Jie, J. Ultrafast, Broadband Photodetector Based on MoSe₂/Silicon Heterojunction with Vertically Standing Layered Structure Using Graphene as Transparent Electrode. *Adv. Sci.* **2016**, *3*, 1600018. [CrossRef]
28. Chang, K.; Chen, W. Single-Layer MoS₂/Graphene Dispersed in Amorphous Carbon: Towards High Electrochemical Performances in Rechargeable Lithium Ion Batteries. *J. Mater. Chem.* **2011**, *21*, 17175–17184. [CrossRef]
29. Xu, D.; Chen, L.; Su, X.; Jiang, H.; Lian, C.; Liu, H.; Chen, L.; Hu, Y.; Jiang, H.; Li, C. Heterogeneous MoSe₂/Nitrogen-Doped-Carbon Nanoarrays: Engineering Atomic Interface for Potassium-Ion Storage. *Adv. Funct. Mater.* **2022**, *32*, 2110223. [CrossRef]
30. Shen, Q.; Jiang, P.; He, H.; Chen, C.; Liu, Y.; Zhang, M. Encapsulation of MoSe₂ in Carbon Fibers as Anodes for Potassium Ion Batteries and Nonaqueous Battery–Supercapacitor Hybrid Devices. *Nanoscale* **2019**, *11*, 13511–13520. [CrossRef]
31. Ge, P.; Hou, H.; Li, S.; Yang, L.; Ji, X. Tailoring Rod-Like FeSe₂ Coated with Nitrogen-Doped Carbon for High-Performance Sodium Storage. *Adv. Funct. Mater.* **2018**, *28*, 1801765. [CrossRef]
32. Wang, G.; Xiong, X.; Xie, D.; Lin, Z.; Zheng, J.; Zheng, F.; Li, Y.; Liu, Y.; Yang, C.; Liu, M. Chemically Activated Hollow Carbon Nanospheres as a High-Performance Anode Material for Potassium Ion Batteries. *J. Mater. Chem. A* **2018**, *6*, 24317–24323. [CrossRef]
33. Atangana Etogo, C.; Huang, H.; Hong, H.; Liu, G.; Zhang, L. Metal–Organic-Frameworks-Engaged Formation of Co_{0.85}Se@C Nanoboxes Embedded in Carbon Nanofibers Film for Enhanced Potassium-Ion Storage. *Energy Storage Mater.* **2020**, *24*, 167–176. [CrossRef]
34. Liu, P.; Han, J.; Zhu, K.; Dong, Z.; Jiao, L. Heterostructure SnSe₂/ZnSe@PDA Nanobox for Stable and Highly Efficient Sodium-Ion Storage. *Adv. Energy Mater.* **2020**, *10*, 2000741. [CrossRef]
35. Wang, J.; Polleux, J.; Lim, J.; Dunn, B. Pseudocapacitive Contributions to Electrochemical Energy Storage in TiO₂ (Anatase) Nanoparticles. *J. Phys. Chem.* **2007**, *111*, 14925–14931. [CrossRef]
36. Cao, B.; Zhang, Q.; Liu, H.; Xu, B.; Zhang, S.; Zhou, T.; Mao, J.; Pang, W.K.; Guo, Z.; Li, A.; et al. Graphitic Carbon Nanocage as a Stable and High Power Anode for Potassium-Ion Batteries. *Adv. Energy Mater.* **2018**, *8*, 1801149. [CrossRef]
37. Zhang, W.; Ming, J.; Zhao, W.; Dong, X.; Hedhili, M.N.; Costa, P.M.F.J.; Alshareef, H.N. Graphitic Nanocarbon with Engineered Defects for High-Performance Potassium-Ion Battery Anodes. *Adv. Funct. Mater.* **2019**, *29*, 1903641. [CrossRef]
38. Shen, W.; Wang, C.; Xu, Q.; Liu, H.; Wang, Y. Nitrogen-Doping-Induced Defects of a Carbon Coating Layer Facilitate Na-Storage in Electrode Materials. *Adv. Energy Mater.* **2015**, *5*, 1400982. [CrossRef]
39. Lu, H.; Wu, L.; Xiao, L.; Ai, X.; Yang, H.; Cao, Y. Investigation of the Effect of Fluoroethylene Carbonate Additive on Electrochemical Performance of Sb-Based Anode for Sodium-Ion Batteries. *Electrochim. Acta* **2016**, *190*, 402–408. [CrossRef]

Disclaimer/Publisher’s Note: The statements, opinions and data contained in all publications are solely those of the individual author(s) and contributor(s) and not of MDPI and/or the editor(s). MDPI and/or the editor(s) disclaim responsibility for any injury to people or property resulting from any ideas, methods, instructions or products referred to in the content.